nature nanotechnology

SUPPLEMENTARY INFORMATION

https://doi.org/10.1038/s41565-017-0019-5

In the format provided by the authors and unedited.

Direct-current triboelectricity generation by a sliding Schottky nanocontact on MoS_2 multilayers

Jun Liu[1]*, Ankur Goswami[1], Keren Jiang[1], Faheem Khan[1], Seokbeom Kim[2], Ryan McGee[1], Zhi Li[1], Zhiyu Hu[3], Jungchul Lee[2] and Thomas Thundat[1,3,4]*

[1]Department of Chemical and Materials Engineering, University of Alberta, Edmonton, Alberta, Canada. [2]Department of Mechanical Engineering, Sogang University, Seoul, Korea. [3]National Key Laboratory of Science and Technology on Micro/Nano Fabrication, Department of Micro/Nano Electronics, Shanghai Jiao Tong University, Shanghai, China. Present address: [4]Department of Chemical and Biological Engineering, University at Buffalo, The State University of New York, Buffalo, NY, USA. *e-mail: jun11@ualberta.ca; Thundat@ualberta.ca

Supplementary Information

Direct-current triboelectricity generation by sliding-Schottky nanocontact on MoS_2 multilayers

Jun Liu, Ankur Goswami, Keren Jiang, Faheem Khan, Seokbeom Kim, Ryan McGee, Zhi Li, Zhiyu Hu, Jungchul Lee and Thomas Thundat

E-mail: jun11@ualberta.ca (Jun Liu), thundat@ualberta.ca (Thomas Thundat)

1. Material characterization

1.1 Scanning electron microscopy (SEM) characterization

SEM characterization was conducted with a Zeiss Sigma 300 VP-FESEM. It has been reported that MoS_2 can be successfully deposited on Ag using PLD, while other metallic materials such Al, Ni, Cu show poor capabilities as substrates.[1] From Fig. S1, MoS_2 grains with good crystal quality are discernible. Hexagonal shape of MoS_2 is evident in the magnified image, which is in line with the AFM results in main text.

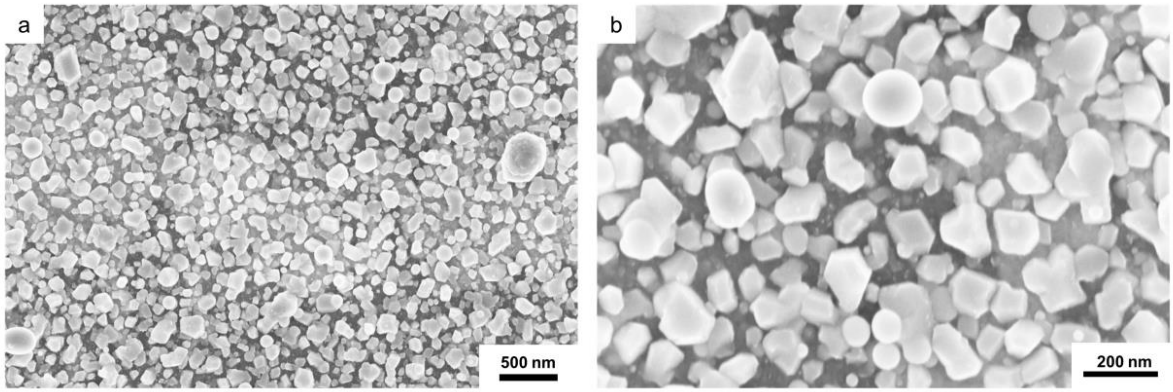

Figure S1. SEM image of MoS_2 thin film deposited by PLD.

1.2 Raman spectra characterization

Raman spectroscopy characterization was conducted with a Thermo Nicolet Almega XR Raman Microscope. The observed peaks correspond to the E and A_{1g} mode oscillation of Mo-S bonding.[1]

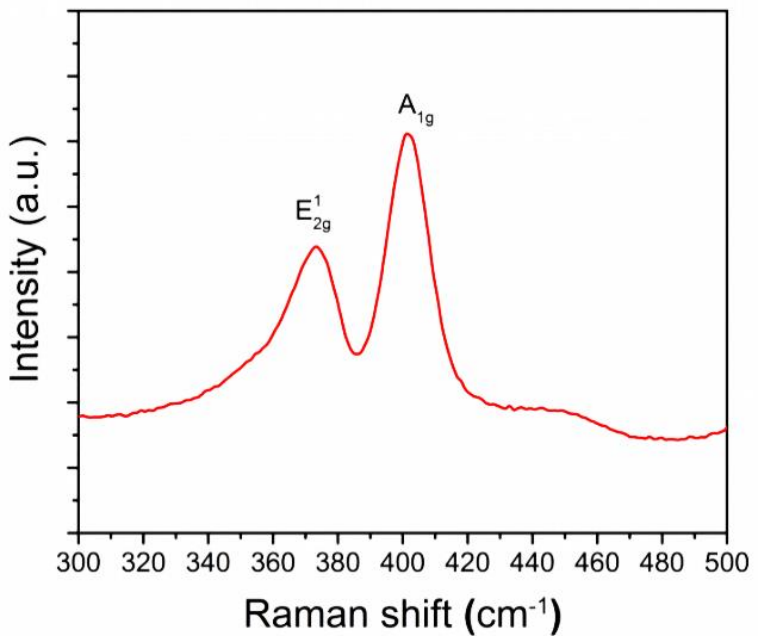

Figure S2. Raman spectra of MoS_2 thin film deposited by PLD.

1.3 X-ray photoelectron spectroscopy (XPS) characterization

XPS characterization was conducted with a Kratos AXIS 165. The collected spectra were analyzed by using the CasaXPS software package. As shown in Fig. S3, the doublet Mo^{4+} $3d_{5/2}$ and Mo^{4+} $3d_{3/2}$ peak located at 229.6 eV and 237.8 eV are attributed to the Mo^{4+} state in MoS_2 (marked as orange).[1,2] Doublet peaks at 232.7 eV and 235.9 eV are attributed to the Mo^{6+} state of MoO_3 (marked as blue).[2,3] S 2s core level peak at 226.7 eV and 228.4 eV corresponds to the S^{2-} state in MoS_2 (marked as purple) and other surface S species such as oxysulfide compounds and SH species (marked as green), respectively.[2] When exposed to air, S vacancies on the PLD-synthesized MoS_2 thin film surface may react with atmospheric oxygen, which give rise to the formation of MoO_3.[3] The observed non-uniform current distribution for the single grain as shown Fig. 1f, may be due to stoichiometry fluctuation on MoS_2 surface as revealed by the XPS result. The existing surface Mo oxide species would degrade the electrical conductivity of those regions.

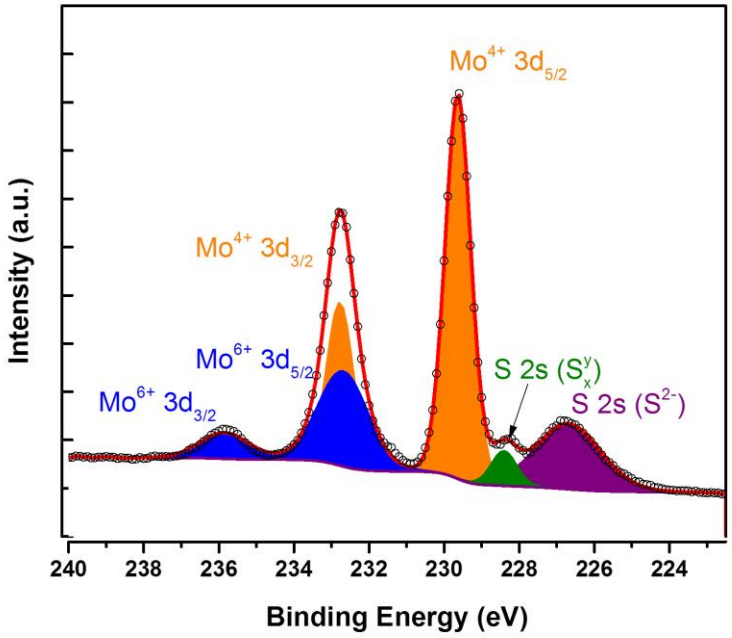

Figure S3. Decomposition of Mo 3d and S 2s XPS peaks of MoS_2 thin film deposited by PLD. Black hollow circles are raw data points. Red solid curve is the fitted result.

2. Artifact exclusion

2.1 Current amplifier calibration

The conductive AFM module has been calibrated by using a standard 100 MΩ resistor provided by the manufacturer. In a typical procedure, the AFM probe was false engaged and a ramping test bias was applied to the C-AFM module. It can be seen from Fig. S4 that the slope of *I*-*V* curve matches perfectly with the standard resistor, indicating no data magnification from analysis.

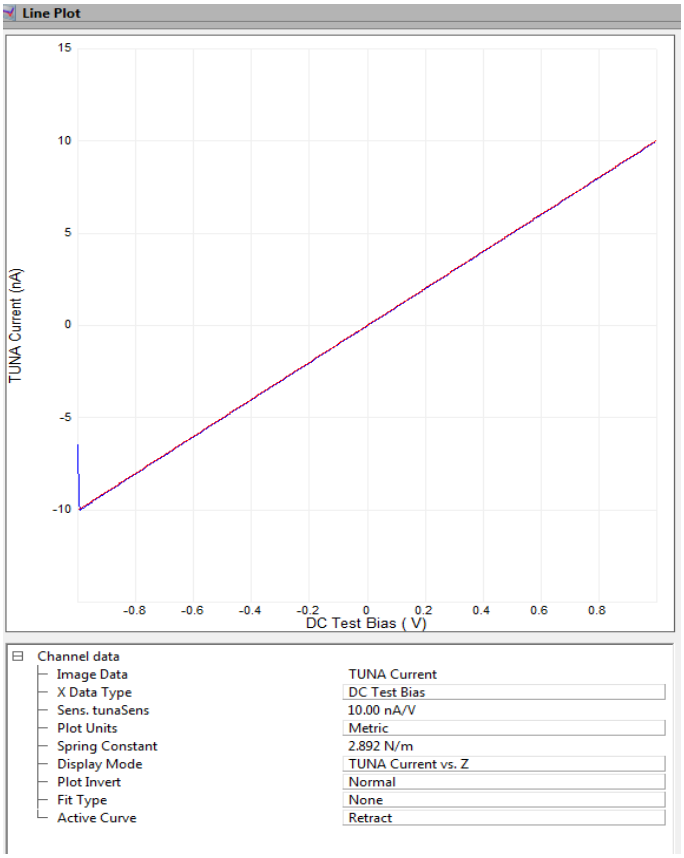

Figure S4. *I-V* characterization with a 100 MΩ standard calibration resistor.

2.2 False engagement

Upon false engagement, AFM probe scans above the sample surface without actual contact, in which case the system noise level can be investigated. It can be seen from Fig. S5 that the noise level in our experiment is around several pA, three orders smaller than the nA current signal upon contact scanning.

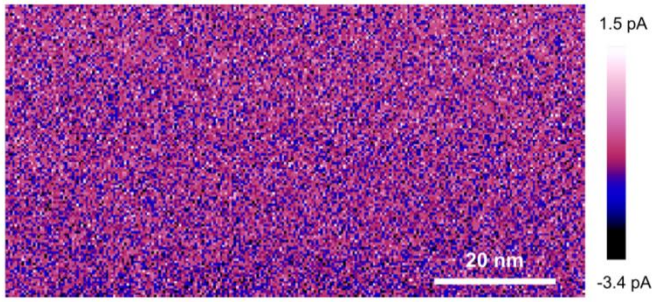

Figure S5. C-AFM current signal under false engagement

2.3 Laser spot position

To exclude to the effect of AFM laser irradiation on the observed C-AFM current, we investigated the laser position–dependent current signal. As shown in Fig. S6, the C-AFM current signal is not sensitive to the laser spot position. As a matter of fact, the AFM laser spot is blocked by the AFM cantilever body, and reflected by the Pt/Ir coating on the top surface of cantilever.

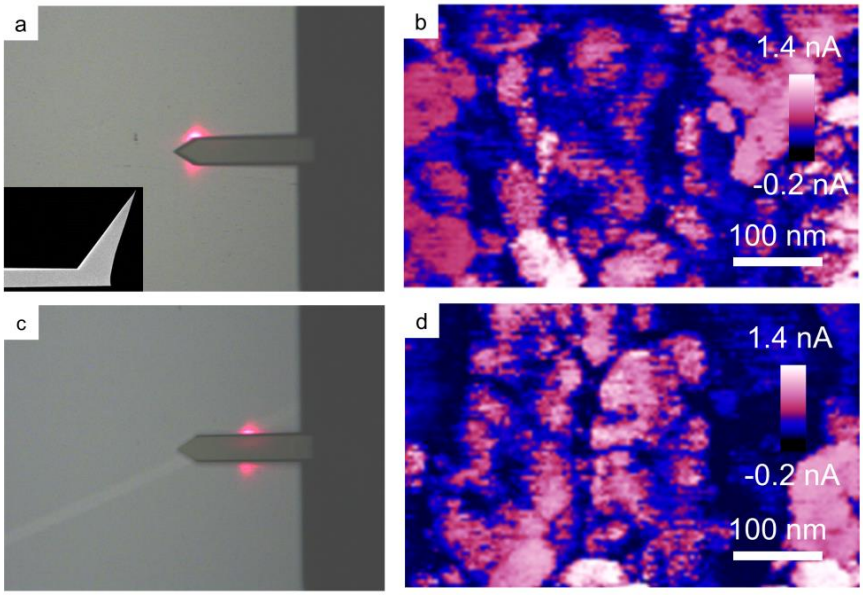

Figure S6. Laser position-dependent C-AFM signal on MoS_2. (a) and (b) are optical images of the AFM cantilever with different laser position. (b) and (d) are the corresponding C-AFM current mapping. Contact force F=5 nN.

3. C-AFM measurement on other materials

3.1 Ag and SiO_2

We have conducted C-AFM experiments on Ag and SiO_2 sample for comparison. As shown in Fig. S7, no current signal has been found on these samples. The electron-hole pairs excited in metal-metal frictional contact has much shorter life time and may just quickly decay into heat. As for insulator SiO_2, charge mobility is very low on the surface and the series resistance is very high that inhibit the DC current flow.

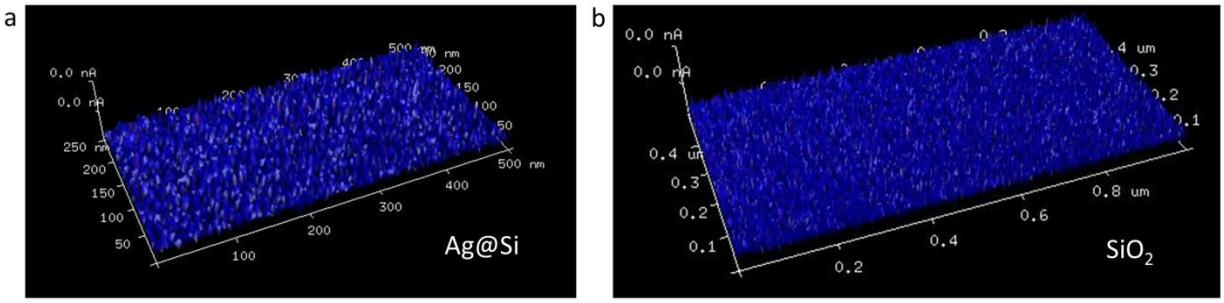

Figure S7. C-AFM current measured on (a) Ag sample and (b) SiO_2 sample.

3.2 P-type Si

The current signal was not observed mainly because of the naturally grown insulating silica on Si surface, and the localized pressure applied by AFM tip may not be able to penetrate and affect the electronic structure at the SiO_2/Si interface.

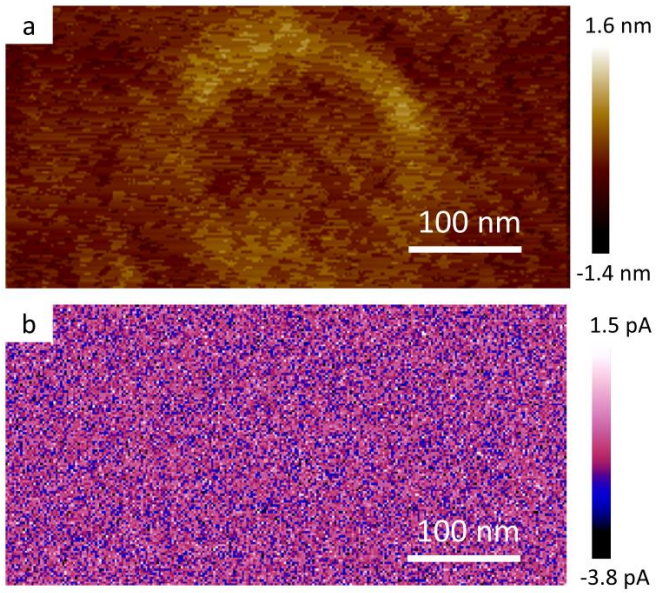

Figure S8. C-AFM measurement on p-type Si. (a) Topography and (b) current map.

3.3 PEG polymer

For comparison, we have also conducted C-AFM measurement on a spin-coated PEG polymer thin film on Au substrate. As shown in Fig. S9, no current signal can be observed. This is mainly because of the poor mobility of tribo-induced charges on the insulating surface.

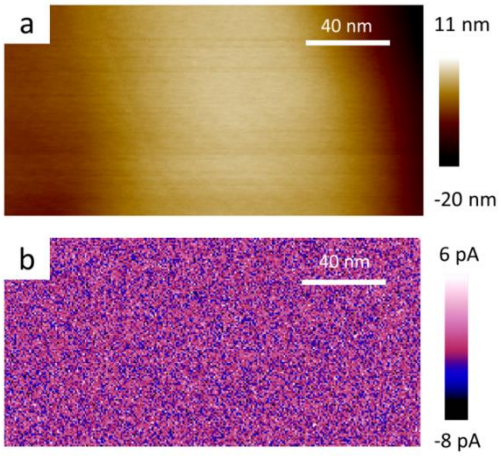

Figure S9. C-AFM current measured on spin-coated PEG polymer thin film on Au substrate. (a) Topography and (b) current map.

4. The proposed charge transfer mechanism

As is shown in Fig. S10, the electrons with sufficient energy may be excited from the surface states or valence band into the conduction band, overcome the energy barrier from semiconductor side (qV_{bi}) and transmit into the metal side. This scenario is very likely to happen since the band gap of layered-MoS_2 is very narrow (1.2-1.4 eV)[4] while the direct electronic excitation from friction can result in highly energetic electron-hole pairs. For the excited electrons with lower energy, they may, if not recombined with the holes, fall into the unoccupied surface states and transmit into the metal side assisted by the intensive electric field and frictional heat. The possible excitations from the metal side, in contrast, would be expected to decay much faster into lattice vibration considering the short lifetime of electron-hole pairs in metal and the higher energy barrier (Φ_B) the excited electrons would meet from the metal side. As a result, a rectification of charge flow can be achieved. It is noteworthy that the surface energy states would inevitably exist in the metal-MoS_2 Schottky contact, due to the surface defects as well as the unusual interface dipole formation[5] (the formation of gap energy states with Mo *d*-orbital characters).

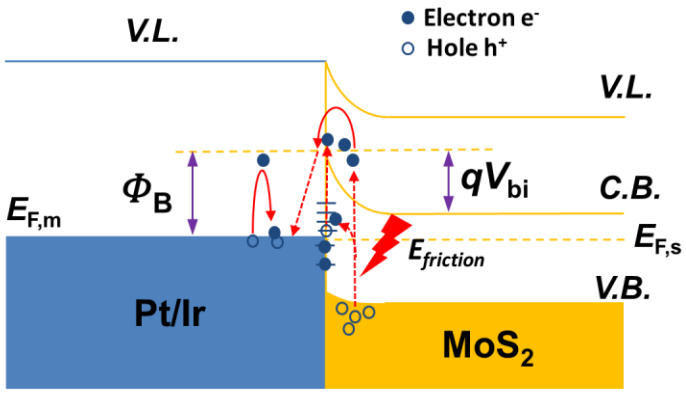

Figure S10. Energy band diagram of the tip-sample interfaces and the proposed charge transfer mechanism: Schottky contact is formed between the Pt/Ir coated AFM tip and MoS_2. While the electrons from surface states/valence band may be excited by frictional energy and transmit into the metal side, the excited electron-hole pairs from the metal side have shorter life time and encounter higher energy barrier.

5. Cyclic *I-V* measurement

The existence of surface S vacancies and other defects facilitate the surface energy states formation, which may store charges as revealed by the observed hysteresis in the cyclic voltammetry measurement (Fig. S11). It is found that the hysteresis loop is much more conspicuous in the case of Cu probe in direct contact with the MoS_2 sample compared with that with a thin Pt/Cr top electrode deposited in advance.

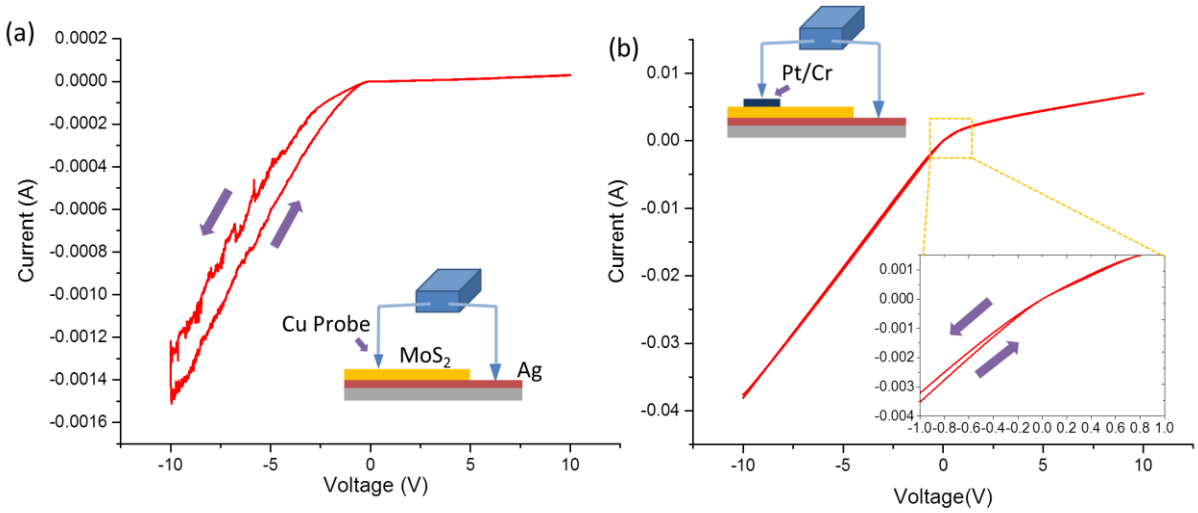

Figure S11. Cyclic *I-V* measurement on the PLD-synthesized MoS_2/Ag sample using probe station. (a) Sample surface in direct contact with Cu probe. (b) Pt/Cr top electrode was deposited in advance and in contact with the Cu probe.

6. C-AFM *I-V* data analysis

The *I-V* data fitting with thermionic emission model is shown in Fig. S12, and the predicted parameters are summarized in Table S1. For region 1 and 2, contact is formed in the order of metal-semiconductor and semiconductor-metal, so that the "forward" direction of Schottky contact, where electron flows from n-type MoS_2 to metal, is opposite in these two cases. Accordingly, fitting was conducted in the positive and negative sample bias part of data acquired in region 1 and region 2, respectively. For region 2, data point #17 has not been considered for fitting since it exhibits an Ohmic feature. Specifically, imperfect fitting of data points #16 and 18 is in line with the existence of tunneling component in the overall charge transport characteristics as discussed in main text.

For the TE model used in our experiment:

$$I = I_0 \exp\left(\frac{eV}{nkT}\right) = AA^*T^2 \exp\left(-\frac{\Phi_B}{kT}\right)\exp\left(\frac{eV}{nkT}\right), A^* = 4\pi q m^* k/h^3 \quad \text{(S1)}$$

metal-semiconductor contact area A=6 nm^2; elementary charge q=1.6×10^{-19} C, effective mass m^*=0.5m_e=4.56×10^{-31} kg, Boltzmann constant k=1.38×10^{-23} J/K, Plank constant h=6.6 × 10^{-34} m^2kgs^{-1}, temperature T=298 K.

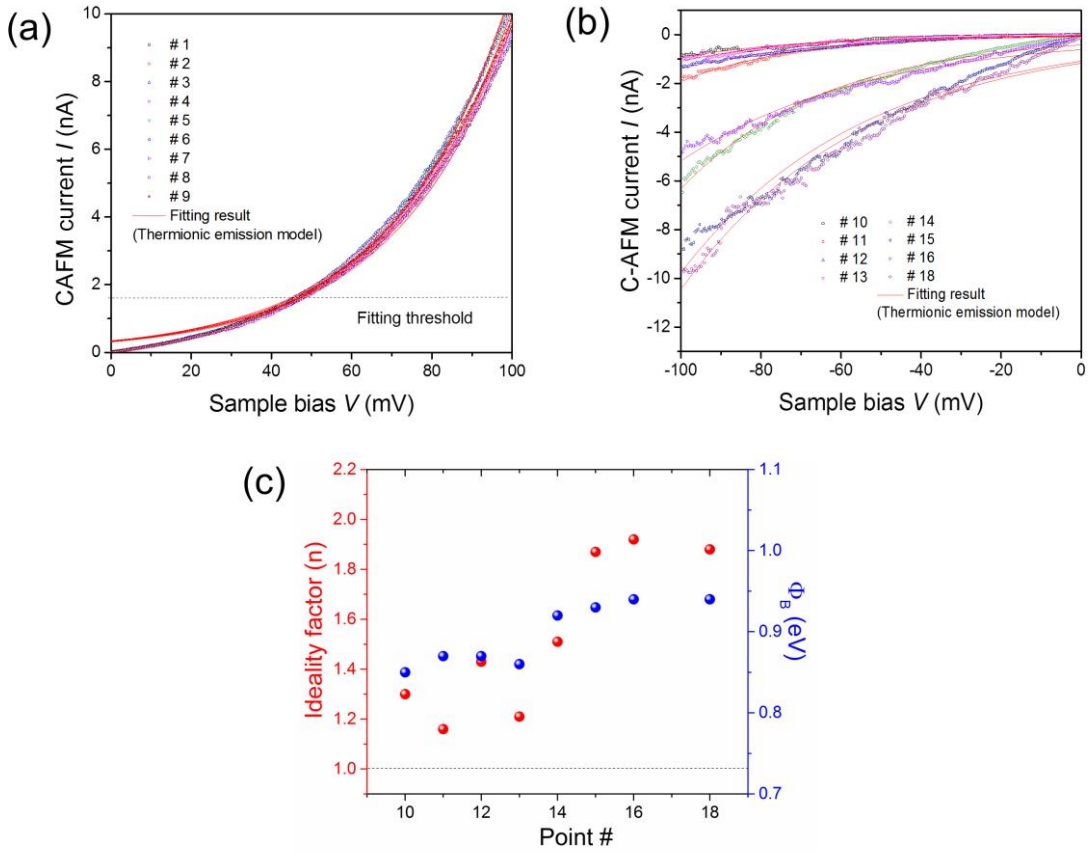

Figure S12. (a) Forward *I*-*V* spectrum (#1-9) fitted with thermionic emission model (eq. 1). (b) Reverse *I*-*V* spectrum (#10-18) fitted with thermionic emission model. (c) Estimated ideality factor *n* and energy barrier Φ_B from fitting result in (b).

Table S1. Summary of fitting results.

Region	Data point #	Ideality factor n	Energy barrier Φ_B (eV)
1	1	1.21	0.89
	2	1.18	0.88
	3	1.18	0.89
	4	1.20	0.89
	5	1.18	0.89
	6	1.19	0.89
	7	1.19	0.88
	8	1.21	0.89
	9	1.19	0.89
2	10	1.30	0.83
	11	1.16	0.84
	12	1.43	0.85
	13	1.21	0.83
	14	1.52	0.89
	15	1.87	0.92
	16	1.92	0.90
	18	1.88	0.92

Fig. S13 provides another typical example. It can be seen that different region of the same grain exhibits different current output. The *I-V* characteristics of the data points confirm the importance of forming proper Schottky contact between the tip and sample.

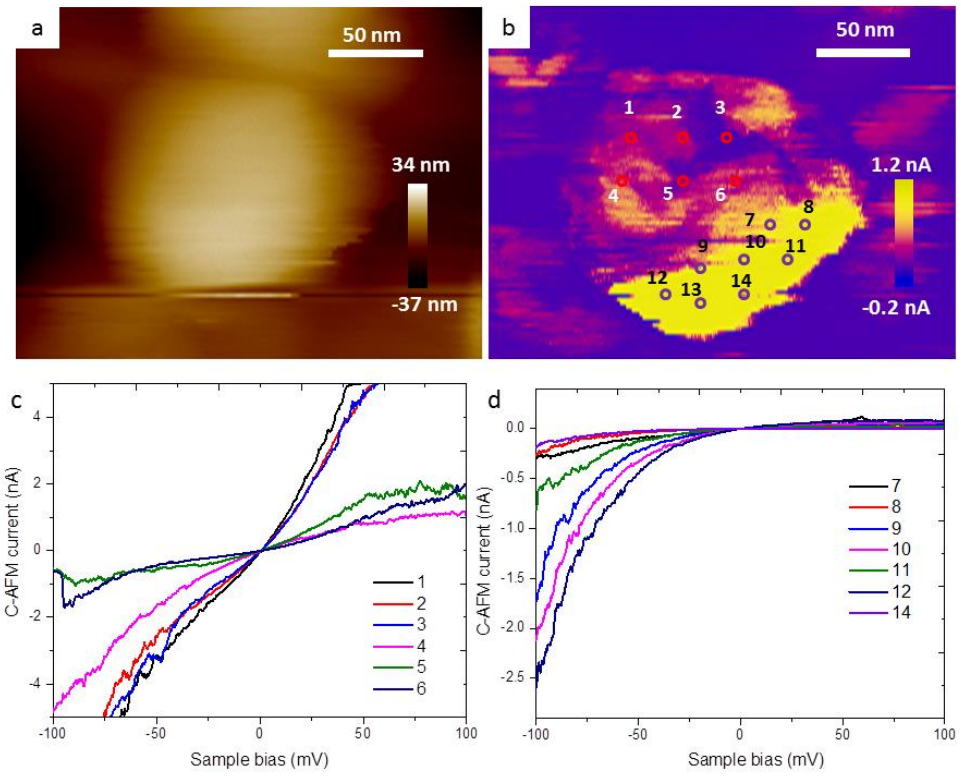

Figure S13. (a) AFM topographic image of one MoS_2 grain and its (b) corresponding C-AFM current map. (c) and (d) shows the *I-V* spectra of the location #1-14 as marked in (b).

7. Contact area estimation

In an AFM system, hard and poorly adhesive materials are best approximated by the DMT model.[6] According to the DMT model, A is given by[6]:

$$A = \pi \left[\frac{R}{K}(L + 2\pi R\gamma)\right]^{2/3} \qquad \text{(S2)}$$

where R is AFM tip radius, L is the load (contact force F), and γ is the work of adhesion. The term $2\pi R\gamma$ can be considered as an 'additional load' L_{ad}, which is determined by the "pull-off" force in the force curve (see Fig. S14). K is the reduced Young's modulus given as $K = \frac{3}{4}\left(\frac{1-\nu_s^2}{E_s} + \frac{1-\nu_t^2}{E_t}\right)$, where E_t and E_s are Young's moduli and ν_t and ν_s are the Poisson ratios of the tip and the sample, respectively. Adhesion measurement was conducted with PeakForce QNM mode (Bruker, USA). The average adhesive force can be used for tip-sample contact area estimation.

For the macroscale demonstration, additional adhesion can be neglected, thus A is approximated by Hertz model[6]:

$$A = \pi \left(\frac{RL}{K}\right)^{2/3} \qquad \text{(S3)}$$

Here, E_t= 165 GPa, ν_t= 0.22 is adopted for the AFM tip, E_t= 79 GPa, ν_t= 0.42 is adopted for gold-coated metallic connector, and E_t= 240 GPa, ν_t= 0.27 is adopted for MoS_2 thin film. In the macroscale demonstration, the applied load L can be roughly estimated to be in the order of 1~10 N by hand.

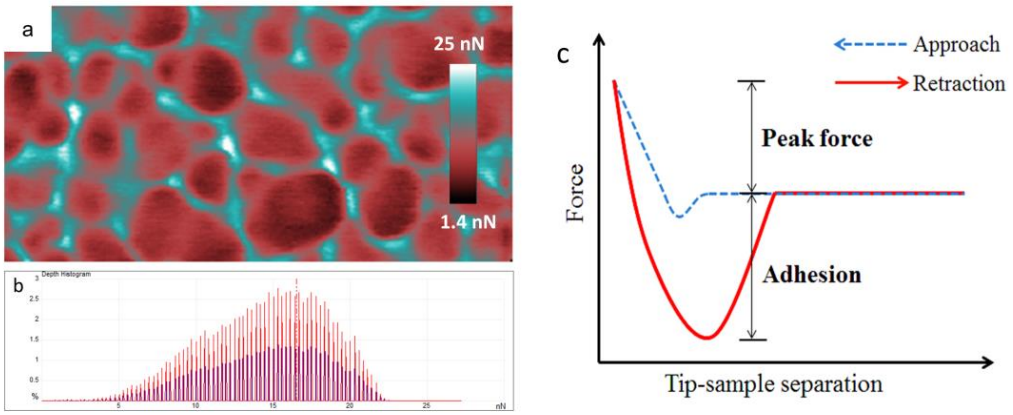

Figure S14. (a) Tip-sample adhesion mapping of MoS_2. (b) Histogram of the adhesion distribution. (c) Typical force curve in PeakForce QNM measurement.

8. C-AFM *F-Z*, *I-Z* characterization

Typical approach (black) and retract (red) curves are shown in Fig. S15. Different stages are depicted in Fig. S15 (a): when the AFM tip approaches the sample, it would snap onto the sample surface due to van der Waals forces.[7] Thereafter, the tip presses on the sample leading to cantilever deflection (elastic deformation). Accordingly, normal force applied on the sample surface can be calculated by the product of cantilever deflection error and spring constant *k*. When retracted again, the tip would stick to the sample surface due to adhesion forces before finally snapping free. The hysteresis between the approach and retract curves is called contact hysteresis caused by friction effects between the tip and the sample.[8] As revealed by the C-AFM current signal in the time domain, charge flow occurs immediately after the tip engagement, enhanced with increasing force and eventually tends to saturate. It should be noted that the current signal (in the order of 10 pA) detected in force curve measurements is much less than that

observed during scanning (in the order of 1 nA) under the same applied force (in the order of 10 nN). Interestingly, two different stages of current signal with response to normal force can be found (Fig. S15 (b) and (d)), which may be related to the existence of less conductive surface depletion regions.

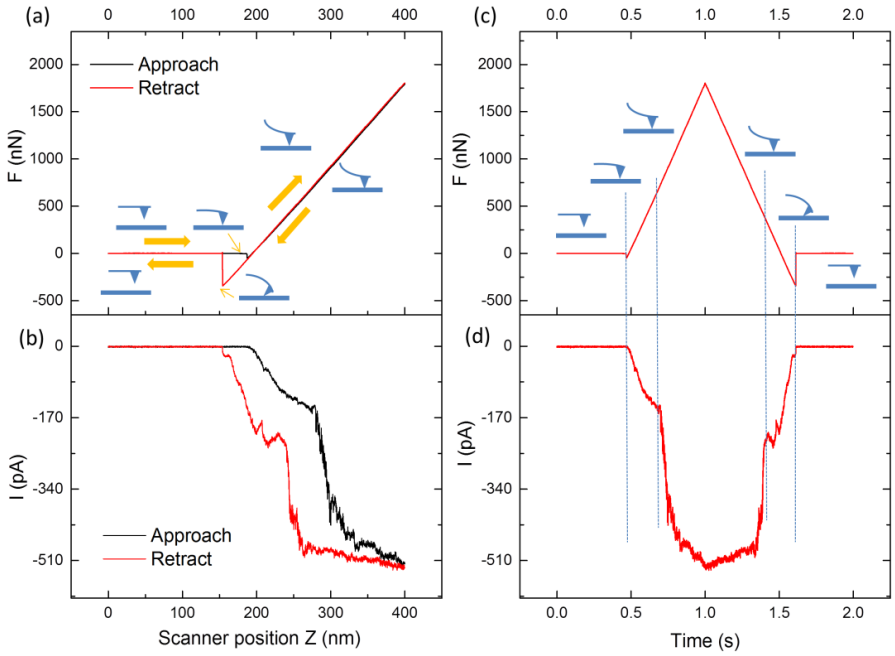

Figure S15. (a) and (b) are AFM cantilever force *F* vs. Piezo-scanner position *Z* and C-AFM current *I* vs. *Z*, respectively. (c) and (d) are their corresponding graphs in time domain.

9. Scan number-dependent C-AFM measurement

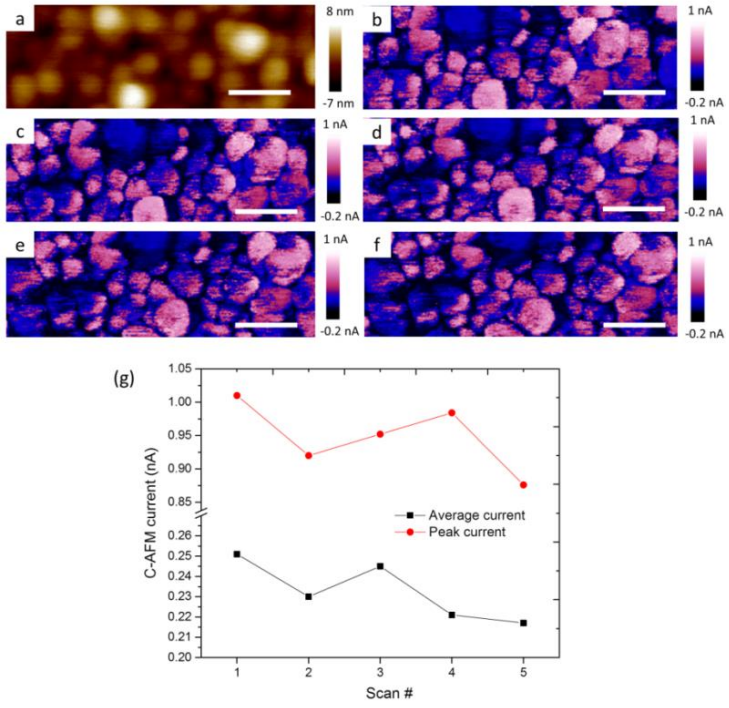

Figure S16. (a) Topography of MoS_2 sample and (b-f) its corresponding current output for multiple scans (#1-5). (The scanned area has little drift during the multiple scanning). (g) Average and peak C-AFM current as a function of scan #.

10. Velocity-dependent C-AFM current

Fig. S17 shows the velocity-dependent experimental data. The velocity range is limited by the piezoelectric actuator in the AFM probe holder. For the investigated range, it is found that the C-AFM current has a slightly decreasing tendency with increasing velocity. This can be a result of current diminishing with multiple scans as shown in Fig. S16, or the tip-sample electrical contact cannot be built up properly within shorter contact time.

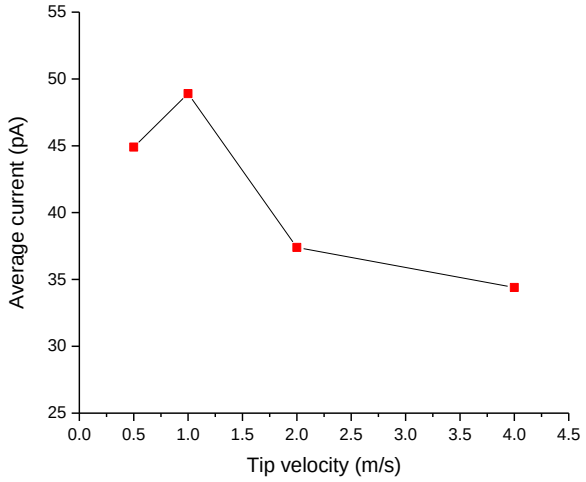

Figure S17. Velocity-dependent C-AFM current data. *F*=5 nN.

11. C-AFM measurement on the exfoliated MoS_2 sample

In comparison, we have also conducted C-AFM measurement on the exfoliated MoS_2 single crystal layers. As is shown in Fig. S18, C-AFM current can be observed on three different MoS_2 layers. The thickness of the very bottom layer is close to that of single layer as revealed by edge topographic scan (Fig. S18g and S18h). It is found that the DC current signal increases with increasing layer thickness, which cannot be explained by conventional TENG theory (AC output) or piezoelectric signal (only occurs and decreases in the order of 1st, 3rd and 5th layer).[9] The current output is much lower than that observed in PLD-deposited MoS_2 samples, indicating possible influence from bottom electrode contact or surface states. In fact, even the ideal metal-MoS_2 contact has very unusual mechanism of the partial Fermi level pinning caused by interface dipole formation (the formation of gap energy states with Mo *d*-orbital characters).[5]

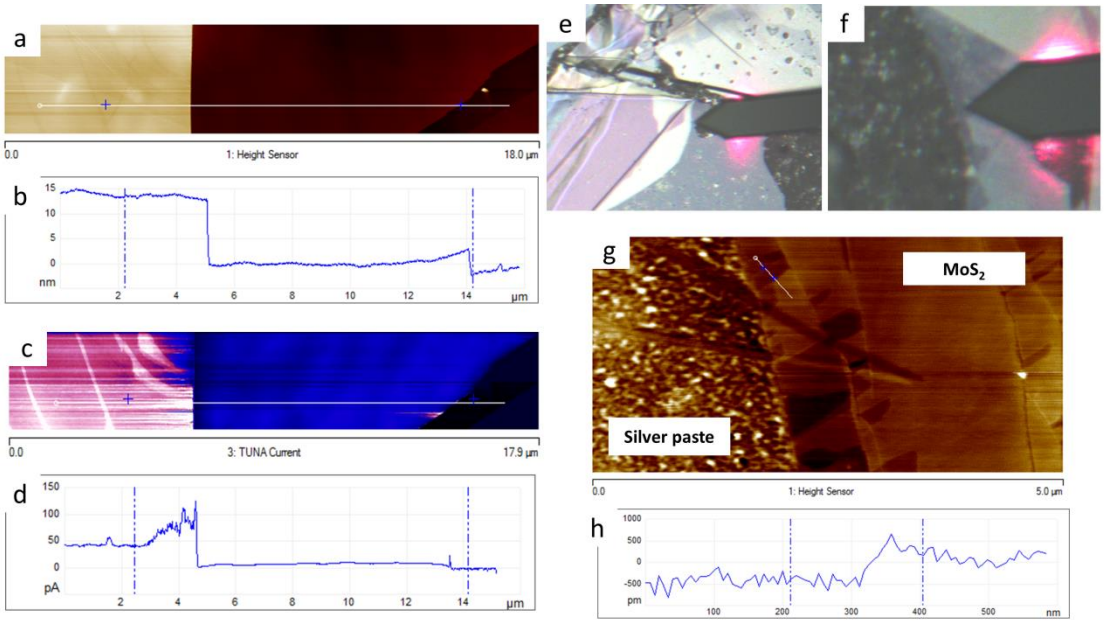

Figure S18. (a) AFM topographic image of exfoliated MoS_2 layers and (c) corresponding C-AFM current map. (b) and (d) show line analysis labeled in (a) and (c), respectively. (e) and (f) are optical microscope images of the scan area of (a) and (g), respectively. (g) AFM topographic image of the silver paste-MoS_2 boundary. From line analysis in (h), atomic layer thickness can be seen.

References

1 Loh, T. A. & Chua, D. H. Growth mechanism of pulsed laser fabricated few-layer MoS2 on metal substrates. *ACS applied materials & interfaces* **6**, 15966-15971 (2014).

2 Bara, C. d. *et al.* Aqueous-Phase Preparation of Model HDS Catalysts on Planar Alumina Substrates: Support Effect on Mo Adsorption and Sulfidation. *Journal of the American Chemical Society* **137**, 15915-15928 (2015).

3 Late, D. J. *et al.* Pulsed laser-deposited MoS2 thin films on W and Si: field emission and photoresponse studies. *ACS applied materials & interfaces* **6**, 15881-15888 (2014).

4 Goswami, A. *et al.* Effect of interface on mid-infrared photothermal response of MoS2 thin film grown by pulsed laser deposition. *Nano Research*, 1-14 (2016).

5 Gong, C., Colombo, L., Wallace, R. M. & Cho, K. The unusual mechanism of partial Fermi level pinning at metal–MoS2 interfaces. *Nano letters* **14**, 1714-1720 (2014).

6 Park, J. Y. & Salmeron, M. Fundamental aspects of energy dissipation in friction. *Chemical reviews* **114**, 677-711 (2013).

7 Butt, H.-J., Cappella, B. & Kappl, M. Force measurements with the atomic force microscope: Technique, interpretation and applications. *Surface science reports* **59**, 1-152 (2005).

8 Hoh, J. H. & Engel, A. Friction effects on force measurements with an atomic force microscope. *Langmuir* **9**, 3310-3312 (1993).

9 Zhu, H. *et al.* Observation of piezoelectricity in free-standing monolayer MoS_2. *Nature nanotechnology* **10**, 151-155 (2015).